

# Lattice correction and commissioning simulation of the Advanced Light Source upgrade storage ring

Thorsten Hellert<sup>✉</sup>, Christoph Steier<sup>✉</sup>, and Marco Venturini

Lawrence Berkeley National Laboratory, Berkeley 94720, California, USA

 (Received 16 February 2022; accepted 26 September 2022; published 15 November 2022)

The ALS-U is the upgrade of the existing Lawrence Berkeley National Laboratory Advanced Light Source to a diffraction-limited soft x-ray light source. Here we present the lattice correction studies and commissioning simulations demonstrating that the proposed machine design can be expected to deliver the intended performance when realistic errors and perturbations are fully accounted for. Critical to this demonstration are the high-fidelity, realistic simulations of the beam-based alignment process (both in turn-by-turn mode during early commissioning and with stored beam) that are now made possible by the *Toolkit for Simulated Commissioning*. In addition to presenting a statistical performance analysis based on a large number of lattice error realizations, we also study the range of further improvements that can be obtained by fine-tuning the correction chain to individual error seeds, mimicking the approach one would follow once the machine is built.

DOI: [10.1103/PhysRevAccelBeams.25.110701](https://doi.org/10.1103/PhysRevAccelBeams.25.110701)

## I. INTRODUCTION

The Advanced Light Source Upgrade (ALS-U) project [1] is underway at the Lawrence Berkeley National Laboratory (LBNL) to replace the existing machine with a diffraction-limited soft x-ray light source. The upgrade is part of the ongoing trend toward a new generation of storage-ring light sources initiated in 2016 with MAX-IV [2], now progressing with the recent commissioning of ESRF-EBS [3] and SIRIUS [4], and to be continued by a number of machines currently under construction or design including, among others, APS-U [5], SLS2 [6], DIAMOND-II [7], SOLEIL upgrade [8], ELETTRA 2.0 [9], and PETRA-IV [10].

The ALS-U Storage Ring (SR) will be an approximately 100 pm natural emittance, 200 m circumference, and 2-GeV energy machine (see Table I). An accumulator ring (AR) required for swap-out injection, similar in size to the SR, will be installed and commissioned first. The AR lattice error analysis and commissioning simulations were reported in [11] using a newly developed simulation tool, the *Toolkit for Simulated Commissioning* (SC) [12], built on Accelerator Toolbox (AT) utilities [13]. In this paper, we apply the *Toolkit* to the SR.

Arguably, lattice error analysis and correction are more critical to the ALS-U SR than to any other new-generation machine currently under consideration. The aggressive

emittance target is met with a nine-bend achromat lattice in an unconventional configuration that enhances the particle-dynamics nonlinearities. Even before errors are factored in, the large nonlinearities naturally result in a small dynamic aperture and, in combination with the relatively low beam energy, short lifetime. The lattice configuration is hybrid-like with dispersion bumps at the two ends of each arc to accommodate the chromatic sextupoles. The tight available space, however, limits the number of chromatic sextupole families to only two. This prevents the compensation of certain higher-order nonlinearities, which would be enabled by a more conventional hybrid or classical high-order MBA design, and requires stronger sextupoles. The combination of strong sextupole and quadrupole magnets makes the machine sensitive to lattice errors, a problem compounded by the low beam energy, which makes insertion-devices (ID) perturbations also important.

The error analysis presented in this paper builds upon [11,14] and validates the lattice design adopted for the ALS-U and demonstrates that, in spite of the beam-dynamic challenges, effective error correction strategies can be devised to reduce further erosion of the small dynamic and momentum aperture and achieve the desired beam quality and operational goals. Among the latter, the goal of a 0.5 h minimum lifetime (set by user-radiation stability requirements, hazard-radiation limitations, and the existing injector-system capacity) is the most significant.

Lattice error modeling, analysis, and correction need to be comprehensive, accurate, and realistic. By realistic, we mean that correction procedures should simulate and represent with fidelity the diagnostic signals available from the control room and the actions that can be taken by the operator. From the start, this was one of the principles that

---

Published by the American Physical Society under the terms of the [Creative Commons Attribution 4.0 International](https://creativecommons.org/licenses/by/4.0/) license. Further distribution of this work must maintain attribution to the author(s) and the published article's title, journal citation, and DOI.

TABLE I. ALS-U storage-ring main parameters.

Electron energy, $E$	2.0 eV
Circumference, $C$	196.51 m
Tune, $\nu_x/\nu_y$	41.358/20.353
Natural chromaticity, $\xi_{0x}/\xi_{0y}$	-64.3/ - 64.8
Chromaticity during operation, $\xi_x/\xi_y$	2/1
Momentum compaction, $\alpha_c$	$2.025 \times 10^{-4}$
Bunch charge, $Q$	1.15 nC
Natural rms emittance, $\epsilon_{x0}$	108 pm rad
Natural rms energy spread, $\sigma_\delta$	$1.02 \times 10^{-3}$
Radiation energy loss/turn (no IDs), $U_0$	245 keV
Damping times, $\tau_x/\tau_y/\tau_z$	5.56/10.7/9.97 ms
Harmonic number, $h$	328
Main rf cavity frequency	500.390 MHz
Main rf cavity voltage	0.6 MV
Synchrotron tune (w/o 3HC, no IDs), $\nu_s$	$1.6 \times 10^{-3}$

inspired the development of the *Toolkit*. The *Toolkit* has undergone substantial updates since its initial publication and application to AR [15]. New features include enhanced capabilities to model fully 6D misalignments [16], more flexible handling of the higher-order multipole field errors, and more realistic correction algorithms.

Systematic multipoles can now be dynamically updated each time the (main or corrector) coil excitation is changed. For the ALS-U SR, this is particularly important since all correctors are embedded in the main magnets and the sextupole multipole errors associated with the correctors are relatively large.

Regarding the correction algorithms, the most important extension is a comprehensive beam-based alignment (BBA) routine. The algorithm is able to perform BBA with turn-by-turn BPM data with only two turns of beam transmission which is critical in early commissioning in order to achieve beam capture. Moreover, the optics correction capability at ALS-U critically depends on the ability to perform BBA on combined function quadrupoles. For both cases, we present a comprehensive investigation into the BBA requirements and capabilities.

After evaluating the commissioning simulation on a large set of 500 error seeds, we study the effect of tailoring the correction chain to individual error seeds and quantify the final performance improvement in a statistically meaningful way.

Besides the ALS-U project, the *Toolkit* is currently being used in the design of ALBA-II [17], DIAMOND-II [18], SOLEIL upgrade [19], ELETTRA 2.0 [20], NSLS-IIU [21], and PETRA-IV [22].

The outline of the paper is as follows: In Sec. II, we give an overview of the ALS-U SR and machine layout, present the relevant error sources, and a first cursory assessment of their effects. A detailed discussion of the BBA routines used in the commissioning simulation is given in Sec. III. The main results of the paper are in Sec. IV where the

complete start-to-finish commissioning process is simulated in its logical order demonstrating the attainment of the desired machine performance. The final Sec. V discusses additional fine-tuning of the error-correction algorithms that can lead to further improvements.

## II. LATTICE AND MACHINE MODEL

### A. Lattice and layout

With straight sections exactly overlapping those of the present-day ALS, the SR layout has an approximate 12-fold symmetry, mildly broken by three pairs of high-field (3.2 T) “hard-bend” permanent-magnet dipoles, each pair located in the middle of an arc every four sectors. All the nine main bends in a “normal” (i.e., without hard bends) sector are combined-function (defocusing) magnets; reverse bending occurs in all the arc focusing quadrupoles located between the main bends. In the sectors where they are present, the single-function hard-bends replace the normal bends no. 4 and 6 and each one is flanked by two thin defocusing quadrupoles contained within the footprint of the normal bend. By design, the betatron-phase advances through all sector arcs are the same. The magnet specifications can be found in Table II.

Injection into the SR is on axis with bunch-train swap-out. During normal operations, 11 trains consisting of 25 or 26 bunches and separated by 10 ns (four empty rf buckets) are stored. About every 30 s, a full train is extracted and replaced with a fresh train from the AR. The extracted train is transferred into the AR where it is replenished with a top-off injection from the booster before the next swap-out cycle. The studies presented here do not include tracking through the AR-to-SR (ATS) transfer line and the simulations begin at the SR injection point. Errors and imperfections accumulated by the beam through the ATS are accounted for by an appropriate specification of the beam’s initial conditions at injection.

A schematic of the lattice including the position of corrector magnets (CMs) and beam-position monitors (BPMs) is shown in Fig. 1. There are 19 BPMs per sector, all suitable for turn-by-turn evaluation. All sextupoles and almost all quadrupoles are adjacent to a BPM. All quadrupoles with the exception of QF1 and QD1 at the two ends of each straight section contain horizontal/vertical dipole correctors and are slightly offset to provide reverse bending. The distribution of girders can be seen in Fig. 2.

All main bending magnets (with the exception of the first and last bend in each arc) have horizontal-dipole trim coils to enable tuning of the quadrupole field strength in a  $\pm 5\%$  range while maintaining the design bending angle. Note that in the simulations the corresponding change of the HCM (horizontal corrector magnet) for a given change in the quadrupole main coil is calculated and applied appropriately each time the set points are changed while realistically considering calibration errors.

In total, 25 horizontal and 18 vertical dipole corrector coils per sector are available; of these, the two pairs on the

TABLE II. Baseline-lattice normal sector specifications for the magnets' effective length  $L$ , bending angle  $\theta$  and field  $B_0$ , quadrupole and sextupole unnormalized  $B'$ ,  $B''$  and normalized  $K_1$ ,  $K_2$  (MAD convention) gradient-field components. All magnets have two counts per sector, except for  $B3$  (five counts per sector). A negative bending angle and  $B$  field indicate reverse bending.

Name	$L$ (m)	$\theta$ (deg)	$B_0$ (T)	Offset [mm]	$K_1$ (m <sup>-2</sup> )	$B'$ (T/m)	$K_2$ (m <sup>-3</sup> )	$B''$ (T/m <sup>2</sup> )
B1	0.34	3.333	1.141	...	-3.000	-20.01	...	...
B2	0.5	3.646	0.849	...	-7.057	-47.08	...	...
B3	0.5	3.763	0.876	...	-7.057	-47.08	...	...
QF1	0.18	...	...	...	13.77	91.85	...	...
QF2	0.19	-0.0914	-0.056	-0.824	10.22	68.20	...	...
QF3	0.115	-0.0062	-0.006	-0.090	10.55	70.36	...	...
QF4	0.305	-0.429	-0.164	-1.609	15.28	101.95	...	...
QF5	0.305	-0.429	-0.164	-1.556	15.79	105.37	...	...
QF6	0.305	-0.429	-0.164	-1.560	15.76	105.16	...	...
QD1	0.14	...	...	...	-13.43	-89.61	...	...
SF	0.28	...	...	...	...	...	1563.	10,430
SD	0.28	...	...	...	...	...	-1280.	8,540
SHH	0.075	...	...	...	...	...	77.72	518.5
SHH2	0.075	...	...	...	...	...	-1156.	7,712

two ends of each straight section (embedded in the harmonic sextupoles) are designed for both slow and fast orbit correction. Skew-quadrupole corrector coils are embedded in all harmonic and chromatic sextupole magnets. In addition, the chromatic sextupoles have normal-quadrupole trim coils for BBA.

The physical aperture model adopted for the lattice-error studies consists of a round chamber with a 6-mm radius everywhere, except for the IDs and the injection/extraction straight section. This is a conservative envelope not

crediting portions of the arc chamber and straight sections where the inner aperture radius is 10 mm. A conservative 3-mm inner-radius round chamber is assumed for all IDs. The vacuum chamber in Sector 1 injection/extraction straight is also slightly conservatively modeled as having a uniform rectangular cross section with 6-mm vertical aperture and [-2 mm, 3 mm] horizontal aperture. Generally, the physical aperture details are not very important since the dynamic aperture (DA) is substantially narrower. In this study, collimators are not included.

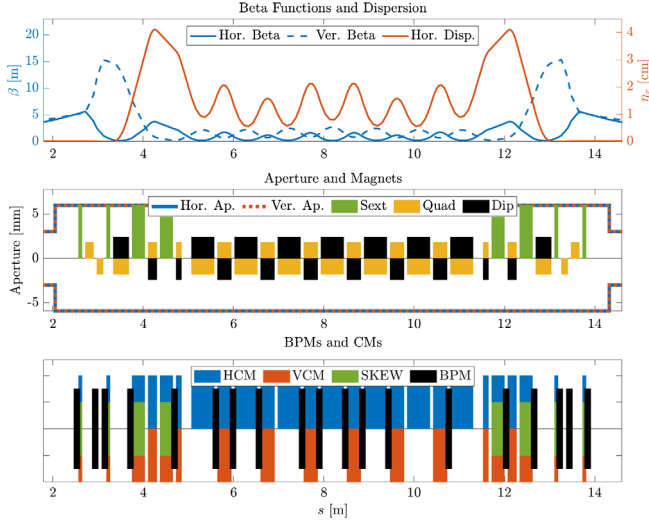


FIG. 1. Lattice and magnet layout in a normal (i.e., without hard bends) sector. Shown are the betatron and the dispersion functions (top), the aperture model, and the distribution of magnets (center) and the distribution of corrector magnets, skew quadrupole correctors, and beam-position monitors (bottom). The center figure emphasizes that all quadrupoles, except for the two pairs at each end, provide some degree of bending.

## B. Error sources

The approach to the lattice-error analysis is similar to the one followed for the ALS-U AR [15]. The assumed error tolerances are specified in Tables III and IV. Random errors are generated following a Gaussian distribution with a  $2\sigma$  cutoff.

*Misalignments.* We consider transverse horizontal and vertical offsets of sectors (full cells), girders, and magnets within one girder as well as longitudinal magnet offsets and girder rolls and magnet rolls around the beam axis. In contrast to other error sources the transverse misalignments of magnets and girders are truncated at  $3\sigma$ .

The implementation of the misalignment modeling is schematically illustrated in Fig. 3. Girder and sector start and end-points each have offset errors. The resulting magnet pitch and yaw angles are calculated with the support structure lengths by assuming a straight line between start and endpoints. The roll error of a magnet is the sum of the individual magnet roll and the roll of the girder on which it is mounted. Similarly, the overall offset of a particular magnet from the design axis is the sum of the offset of the sector relative to its design position, the offset of the girder relative to the sector, and the offset of the magnet relative to the girder.

TABLE III. Magnet misalignments and other errors (rms). Typical error distributions applied in simulations are truncated  $2\sigma$  Gaussians, though magnet and girder transverse misalignments are truncated at  $\pm 3\sigma$ .

Type	rms	Type	rms
Sector transverse offset	100 $\mu\text{m}$	BPM offset	500 $\mu\text{m}$
Girder transverse offset	35 $\mu\text{m}$	BPM roll	4 mrad
Magnet transverse offset	35 $\mu\text{m}$	BPM noise (TbT)	30 $\mu\text{m}$
Magnet roll/pitch/yaw	200 $\mu\text{rad}$	BPM noise (CO)	1 $\mu\text{m}$
Girder rolls	100 $\mu\text{rad}$	BPM calibration	5%
Magnet longitudinal offset	200 $\mu\text{m}$	BPM sum signal	20%
CM calibration	5%	rf voltage	0.1%
Magnet field strength	0.1%	rf phase	180°
Magnet calibration	0.02%	rf frequency	0.1 kHz
Circumference	0.2 mm		

TABLE IV. Storage ring injected-beam rms systematic and jitter errors and rms injected beam sizes.

	Systematic	Jitter		Beam size
$\Delta x$	500 $\mu\text{m}$	10 $\mu\text{m}$	$\sigma_x$	64 $\mu\text{m}$
$\Delta x'$	200 $\mu\text{rad}$	10 $\mu\text{rad}$	$\sigma_{x'}$	31 $\mu\text{rad}$
$\Delta y$	500 $\mu\text{m}$	1 $\mu\text{m}$	$\sigma_y$	7.8 $\mu\text{m}$
$\Delta y'$	200 $\mu\text{rad}$	0.5 $\mu\text{rad}$	$\sigma_{y'}$	2.6 $\mu\text{rad}$
$\Delta E/E$	$1 \times 10^{-3}$	$1 \times 10^{-4}$	$\sigma_\delta$	$1 \times 10^{-3}$
$\Delta\phi$	0	0.1°	$\sigma_\phi$	0°

The chromatic sextupole magnets include quadrupole trim coils to allow for beam-based alignment, see Sec. III B. While only one of the coils is powered at a time and saturation effects are limited, the magnetic centers of the quadrupole and the sextupole field may vary. Simulations not reported here show that this effect can be measured with a stretched wire system on the bench for each magnet to an accuracy of 6  $\mu\text{m}$  rms for each coil. Thus, after BBA is performed on the quadrupole trim coils in the simulations (Sec. IV G), we add this systematic static error to the BBA results.

*Magnet strength.* The main field components of all magnets are assigned a 0.1% rms fractional error. Furthermore, a  $2 \times 10^{-4}$  rms calibration relative error between the set-point change and the actual field is

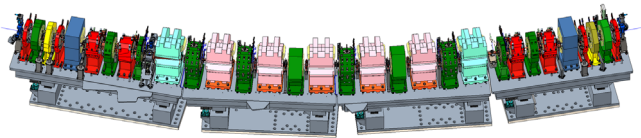


FIG. 2. CAD drawing of a normal arc sector including the four girders (or “rafts”) and their supports. The nine main bends are depicted in blue (B1 type), cyan (B2), and pink (B3). The eight sextupoles are in red. The focusing and defocusing quadrupoles are in green and yellow/light-green, respectively. In the non-normal sectors, normal bends no. 4 and 6 are replaced by permanent-magnet hard bends.

assumed. Horizontal and vertical CMs have a calibration error of 5% rms. Additionally, multipole errors are included as discussed below.

*BPMs.* BPM errors considered in the commissioning simulation include calibration errors as well as rolls around the beam axis, offsets, noise for a single pass, and the stored beam reading. The value for the single pass noise presupposes a bunch charge of 0.4 nC, conservatively smaller than the design 1.15-nC charge/bunch. The BPM noise with the stored beam is assuming a beam current of 50 mA, thus 1/10 of the design current.

Similar to the magnet misalignments, the overall BPM offsets and rolls are the sum of the misalignments of the girder and the individual BPM. Nonlinearities or saturation effects are not included. The BPM does not return an offset reading if more than 60% of the injected beam particles are lost and a calibration error of the sum signal of 20% is assumed.

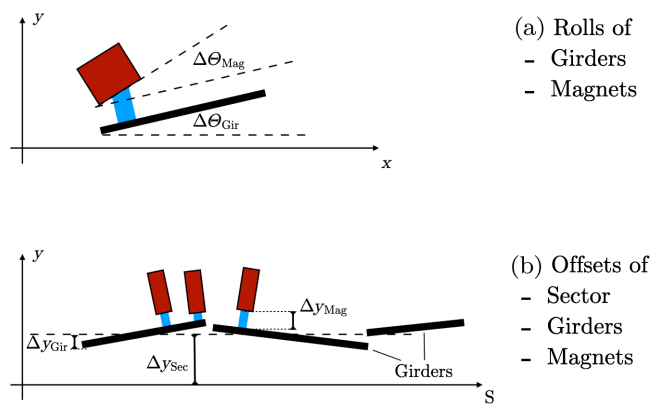


FIG. 3. Illustration of how roll and offset errors stack up in the implementation of the SR misalignment error model. Note that each full sector is assigned an offset, girders in a sector are assigned offsets relative to their sector, and individual magnets are assigned offsets relative to the girder on which they are mounted. The girder yaw and pitch angles are derived from the specification of the offsets at the girder ends.

*Injection.* The injected-beam static and jitter errors are listed in Table IV, reflecting earlier and partly outdated working assumptions. The beam-jitter error numbers, in particular, are now expected to be noticeably larger than those reported here. These are primarily driven by the pulsed elements involved in the swap-out injection. Further work will be needed to assess the effect of larger jitter before the requirements for the pulsed elements' shot-to-shot stability are finalized.

The systematic phase error between the injected beam and the cavity is accounted for by the rf phase error. The injected beam size is calculated assuming a beam with a transverse emittance of 2 nm and 1% coupling and a beta function mismatch of 20%.

*Higher-order multipole errors.* Simulations include the magnets' systematic and random higher-order multipole-field errors with 2D multipole expansion

$$B_y + iB_x = \sum_{n=1} (B_n - iA_n) \frac{(x + iy)^{n-1}}{R^{n-1}}, \quad (1)$$

where  $R$  is the reference radius, with  $n = 1, 2, \dots$  corresponding to the dipole, quadrupole, ..., components. The systematic and random higher-order multipole errors associated with the magnet primary coils are reported in Tables V and VI. The multipole errors for the hard bends and those associated with the corrector coils are reported in the Appendix. The quantities in the tables,  $a_n = A_n/C_{\text{des},m}$ ,  $b_n = B_n/C_{\text{des},m}$ , are the multipoles expressed relative to the design-field component  $C_{\text{des},m}$ . For the quadrupole and

TABLE V. Systematic higher-order multipole errors in units of  $10^{-4}$  (primary coils).

	Q	B1	B2/B3	SHH	SHH2	SF/SD
$b_3$	0	15	-11	...	...	...
$b_4$	0	-4.7	-30	0	0	0
$b_5$	0	-3.3	1.6	-4.9	-2.2	0
$b_6$	-17	1.2	-4.8	0	0	0
$b_7$	0	-1.6	2.4	0.8	0.63	0
$b_8$	0	-2.1	-1.5	0	0	0
$b_9$	0	0.96	0.41	-9.2	-11	-13

TABLE VI. Random higher-order multipole errors in units of  $10^{-4}$  (primary coils).

	Q	B1	B2/B3	S
$a_3/b_3$	3/3	0.7/3.7	0.7/3.7	6.5/6.5
$a_4/b_4$	0.17/1.2	0.4/0.38	0.4/0.38	7/7
$a_5/b_5$	0.13/0.13	0.17/0.17	0.17/0.17	2.8/2.8
$a_6/b_6$	0.027/0.014	0.1/0.1	0.1/0.1	1.2/1.2
$a_7/b_7$	0/0	0.1/0.1	0.1/0.1	0.19/0.19
$a_8/b_8$	0/0	0.1/0.1	0.1/0.1	0.02/0.02

combined-function dipole magnets  $C_{\text{des},2} = B_2$ ; for the sextupole magnets  $C_{\text{des},3} = B_3$ ; for the horizontal and vertical dipole correctors  $C_{\text{des},1} = B_1$  and  $C_{\text{des},1} = A_1$ ; and for the skew quadrupole correctors  $C_{\text{des},2} = A_2$ . For random errors,  $a_n$  and  $b_n$  represent the error distribution rms width. The coefficients in Eq. (1) are related to the AT normalized field coefficients by  $A_n^{\text{AT}} = -A_n/(R^{n-1}B\rho)$ , and  $B_n^{\text{AT}} = B_n/(R^{n-1}B\rho)$ .

The reference radius is  $R = 5$  mm for all magnets (primary and corrector coils) except for the hard bends for which  $R = 3$  mm. The multipoles of the main bending magnets are calculated along the design curved orbit and those of the other magnets along the (straight) magnet axis.

All systematic multipole errors are dynamically updated according to the current excitation of the corresponding main coil. In the simulations, we have no lower-order random multipole errors, on the assumption that these will be measured and corrected before magnet installation.

### C. Performance of the uncorrected lattice

To start to gain some insight into the lattice performance, we studied the particle dynamics in the presence of all the errors included in our model (misalignments, calibration errors, etc.) but before any correction to the orbit or linear optics. This provides an interesting way to draw comparisons with other machines. The study scaled all the errors from Table III by the same multiplicative scaling factor; thus, an error scaling factor of 1 corresponds to the nominal errors.

For each lattice realization, we calculated the rms closed-orbit deviation (COD), the dynamic aperture, and the

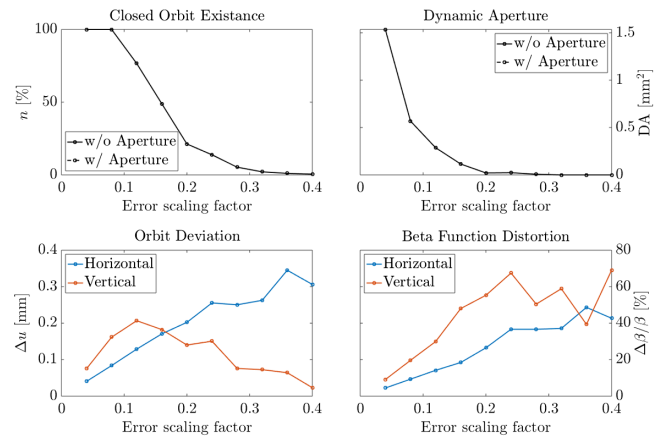


FIG. 4. Lattice properties before correction for different scaling factors of the nominal error set. The plots are the fraction of lattice realizations at which the closed orbit exists (upper left), the rms dynamic aperture (upper right), and the rms closed orbit deviation (lower left) and beta beat (lower right). The calculations in the top images were done with (dashed) and without (solid) physical apertures, but the results are indistinguishable. Note that beta beat and orbit error are only calculated for the cases in which the closed orbit exists.

beta-function distortion  $\Delta\beta/\beta$ . The evaluation was performed with and without the physical aperture model. Results for 500 error realizations are shown in Fig. 4. At about 10% of the nominal error amplitude, the closed orbit exists in nearly 100% of the cases (upper left plot) and drops to virtually zero at an error scaling factor of 0.3. The closed orbit was deemed to exist if the `ATfindorbit6()` function successfully converged to a solution. Note that, in the range of errors considered, the presence of the physical aperture has no visible consequence. Not surprisingly, a comparison with the AR results (see Fig. 9 in [15]) shows a considerably larger sensitivity to errors, emphasizing the importance of an effective orbit and optics correction strategy. A larger sensitivity is also observed in comparison to similar studies performed for APS-U [23].

### III. BEAM-BASED ALIGNMENT

Beam-based alignment (BBA) is a well-established technique [24,25] to effectively calibrate BPMs at the  $10\text{ }\mu\text{m}$  level, well beyond the accuracy made possible by conventional calibration or physical alignment methods. In a machine like the ALS-U SR, this level of accuracy is crucial to achieve successful orbit and linear-optics correction and ultimately avoid DA and momentum aperture (MA) degradation. To do BBA, a BPM is paired with an adjacent quadrupole or sextupole magnet; through controlled closed-orbit perturbations or trajectory steering, one searches for conditions where the beam crosses the magnetic center of the magnet of interest and then registers the reading of the adjacent BPM when that occurs. The BPM readings so obtained will then provide the targets for closed-orbit or trajectory correction.

The implementation details of trajectory and stored-beam BBA are presented in Secs. III A and III B. Special consideration is given to corrector-magnet calibration errors in the reverse-bending quadrupoles (Sec. III C) and the algorithm for automatic outlier detection (Sec. III D). Additional details (e.g., the actual BPM-magnet pairings, etc.) can be found in the commissioning simulation script made available online [26].

#### A. Trajectory beam-based alignment

As shown in the next section, the assumed  $500\text{ }\mu\text{m}$  rms BPM mechanical/electrical alignment is adequate to achieve beam transmission over a few turns, but further progress in the commissioning requires that we know the BPM offset relative to the adjacent magnets' centers with much better accuracy. Before stored-beam BBA (the standard method for beam-aided alignment in storage rings) can be performed, a BBA on the beam trajectory is required, akin to the approach followed in single-pass systems [27].

In the model-independent version that we have adopted, trajectory BBA requires beam transmission through at least

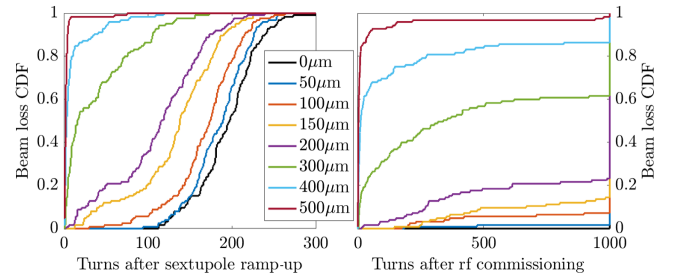


FIG. 5. Beam transmission at two stages of commissioning as described later in Secs. IV A–IV E, after ramping up the sextupole magnets (left) and after rf commissioning (right), assuming various levels of BBA accuracy for the trajectory-based BBA procedure as indicated in the inset. Each curve is the CDF of 100 lattice realizations.

two turns and for simplicity assumes control of the injected-beam trajectory spatial and angular offsets to control the trajectory excursion at the targeted magnet. Trajectory BBA is done with the sextupole magnets off.

To estimate the accuracy requirement for trajectory BBA, we carried out a preliminary simulation of beam transmission in early commissioning (see Secs. IV A–IV E) corresponding to various levels of assigned BPM misalignment ranging from 0 to  $500\text{ }\mu\text{m}$ . The evaluation was done at two stages of commissioning: the first was after the sextupoles are fully powered; the second was after the rf system is also turned on. The results, shown in Fig. 5, indicate that after rf commissioning, with BPM offset errors below  $150\text{ }\mu\text{m}$  rms, about 85% of the cases exhibit at least 1000-turn beam transmission, while this is true for only 1% of the cases with  $500\text{-}\mu\text{m}$  rms offset, see Fig. 6.

In these figures (and other figures later on), each curve represents a cumulative distribution function (CDF). The horizontal axis reading corresponding to  $\text{CDF} = 0.5$  identifies the median of the distribution function. It can be concluded that the BPM offset should be known to about  $50\text{ }\mu\text{m}$  in order to reliably achieve beam capture. The algorithm for trajectory BBA that we have developed and

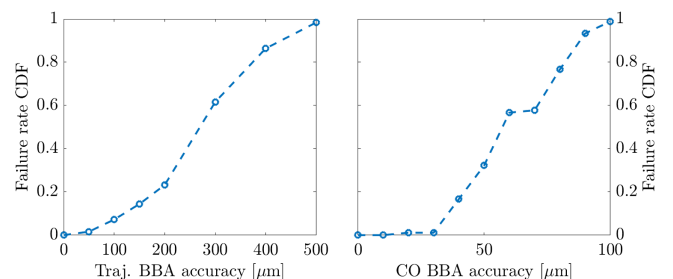


FIG. 6. Correction chain failure rate vs assumed accuracy of the trajectory (left) and closed-orbit BBA (right). For trajectory, BBA failure is defined as not achieving 1000 turns beam transmission after rf commissioning; for closed-orbit BBA as nonconvergence of the linear-optics correction as described in Sec. IV H.

used in the commissioning simulations (Sec. IV B) is described in the following.

BBA requires the ability to vary the trajectory offset at the magnet/BPM of interest over a reasonable range. In principle, the trajectory offset can be adjusted either by powering correctors in the ring or steering the injected beam emerging from the ATS transfer line. Steering is the only option for BBA on the first BPMs past the injection point since there are not enough usable correctors available up to that point. We found that steering the beam at injection remains effective for BBA on all the other BPMs as well; therefore, in our simulations, we have generally adopted this “steering and no-corrector” method.

We assume that we can control the  $x/y$  spatial and angular offsets of the trajectory at the injection point over  $\pm 0.9$  mm and  $\pm 0.9$  mrad ranges. These ranges are centered on the offset errors at injection, as reported in Table IV. In our simulations, we steer the beam by varying the initial spacial offset by  $\Delta U$  (where  $U = X$  or  $Y$ ) and assume that the initial angular offset varies proportionally to  $\Delta U$  with a set proportionality factor. We proceed by injecting the beam with  $+\Delta U$  offset and monitoring the beam transmission; we then repeat with  $-\Delta U$ . If in either case the beam gets lost before the BPM targeted for BBA, we reduce  $\Delta U$  by 10% and repeat until the beam reaches the BPM when lurching with both  $\pm\Delta U$  offsets; this defines  $\Delta U_{\max}$ . If the trajectory excursion at the BPM and the paired magnet is too small, we change the phase advance between the injection point and BPM by tuning one of the quadrupoles in between; the first available quadrupole is  $QF1$  (we assume an 80–105% operational range.) We vary the quadrupole strength within the above range until the difference in the trajectory excursions observed at the BPM for  $+\Delta U_{\max}$  and  $-\Delta U_{\max}$  is larger than a preset target, typically on the order of 0.5 mm.

With this preparation work completed, we are ready to gather the data for BBA. For this purpose, we choose ten equally separated values  $U_j$  in the interval  $[-\Delta U_{\max}, \Delta U_{\max}]$ . We impart these values to the injected beam and for each  $U_j$ , we record the reading  $u_j$  of the targeted BPM and the readings  $u_{j,i}$  of the downstream BPMs, where  $i$  is the BPM index. We repeat the measurement with the quadrupole adjacent to the targeted BPM set at 95% and 105% of its nominal strength. The relevant quantity is the difference  $\Delta u_{j,i}$  of the BPM readings corresponding to the two quadrupole settings. For each BPM data set, we perform a linear regression  $\Delta u_{j,i}$  vs  $u_j$  of the  $j = 1, \dots, 10$  data points and the zero crossing is identified; finally, we weigh the results from all the available downstream-BPM data. The weighted zero-crossing average is our best estimate of the targeted-BPM reading when the beam trajectory crosses the magnetic center of the adjacent quadrupole. For an illustration of BBA data and analysis, see Fig. 7. BBA results within the correction chain are shown later in Fig. 11. In the *Toolkit*, data collection

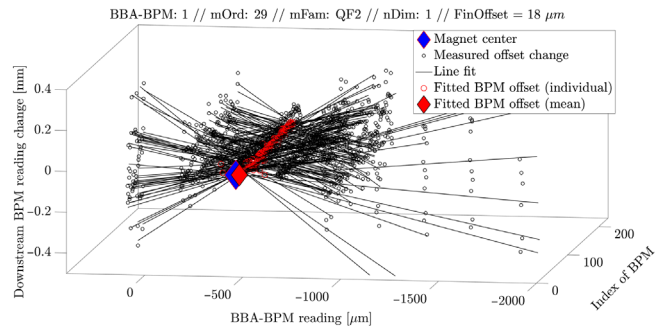


FIG. 7. Illustration of trajectory BBA for the BPM-quadrupole pair BPM4-QF2: data and analysis. The  $x$  axis shows the reading of the BPM targeted for BBA; the  $y$  axis shows the index of the downstream BPMs; and the  $z$  axis the difference in the trajectories as recorded at the downstream BPMs when changing the quadrupole strength from 95% to 105% of the nominal. A black dot represents the measurement for one of the ten steering offsets imparted to the injected beam; the black lines are linear fits. The red dots mark the zero crossing of these lines and the red diamond shows the weighted mean. In this example, the weighted mean is  $19 \mu\text{m}$  off the actual quadrupole center, much less than the physical misalignment between BPM and quadrupole, about  $-500 \mu\text{m}$ . Note that after 12 BPMs downstream of the BBA-BPM, beam transmission decreases significantly when the injected beam is steered too much and only five out of the ten steered trajectories can be utilized; after 189 BPMs, no data could be used for BBA due to beam loss. This figure is conveniently created by switching on a plot flag in the SCBBA() routine.

and analysis are performed in an automated way by the high-level command SCBBA().

## B. Stored-beam BBA

Once a stable closed-orbit is established, stored-beam BBA can be carried out. We distinguish between quadrupole and sextupole magnet BBA.

*BBA on sextupoles.* While errors in the harmonic sextupoles have a relatively modest effect on the beam, ensuring a small closed orbit deviation (COD) in the much stronger chromatic sextupole magnets is crucial for good SR lattice performance. This effect is illustrated in Fig. 8.

The DA and Touschek lifetime were evaluated after performing the full correction chain up to the LOCO-based linear optics correction (see Secs. IV A to IV H) having varied the range of physical misalignments assigned to the BPMs to mimic the effective alignment that could be credited to BBA (the various data-point colors). The realized COD in the sextupoles scales with those ranges. A strong correlation between the beam lifetime in the corrected lattice and the rms COD in the sextupole magnets is clearly visible in the figures. A linear fit to the data yields about  $1.5 \text{ min}/\mu\text{m}$ .

For several reasons, BBA carried out only on the quadrupoles would be inadequate to realize sufficiently small COD in the sextupoles and we found direct sextupole BBA to be

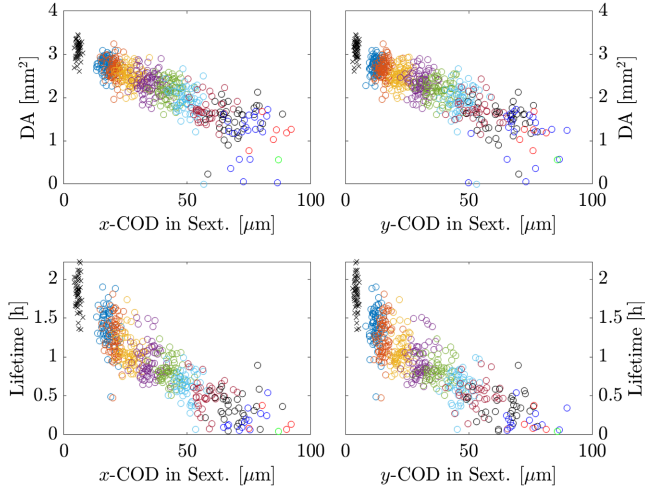


FIG. 8. Scatter plots of DA (top) and Touschek lifetime (bottom) vs rms closed-orbit distortion (COD) in the chromatic sextupole magnets. Left and right plots show the horizontal and vertical CODs, respectively. DA and lifetime are calculated after performing LOCO-based linear optics correction (see Secs. IV A–IV H) for various sets of BBA accuracy assumptions between 0 and 100  $\mu\text{m}$  identified by colored circles. The black crosses are calculated with 0- $\mu\text{m}$  BBA accuracy and 10  $\mu\text{m}$  magnet and girder offsets. Each data point corresponds to one lattice and appears in all four plots. The average lifetime is below the 0.5 h requirement above 60  $\mu\text{m}$  COD. Note that only cases where LOCO converged are shown (see also Fig. 6).

necessary. One reason is that BBA limited to quadrupoles would require reliance on excessively tight magnet-to-magnet magnetic/mechanical alignment. Another reason is that the relevant BPM may be too far from the first usable quadrupole.

We considered two possible BBA solutions: one using the sextupole coils directly and the other using dedicated trim quadrupole coils added to the sextupole magnet. Our simulations show that the latter is preferable, see Table VII. More in detail, the quadrupole trim coils are used to perform BBA on four BPMs adjacent to the four chromatic sextupole magnets per sector. During BBA data collection, the sextupole coils of the targeted sextupole magnet are switched off to avoid saturation effects [2]. The method presupposes that we know the quadrupole-coils' center relative to that of the sextupole coils.

TABLE VII. Achievable accuracy of simulated BBA on sextupole magnets using either the sextupole or the quadrupole trim coils.

	Trajectory BBA ( $\mu\text{m}$ )	Stored-beam BBA ( $\mu\text{m}$ )
Sextupole coils	60	30
Quadrupole trim coils	25	15

As described in Sec. II B, the magnetic centers of the quadrupole and the sextupole field may differ and their center is known with an accuracy of 6  $\mu\text{m}$  rms. Thus, after BBA is performed on the quadrupole trim coils in the simulations, we account for that uncertainty by adding a Gaussian error distribution with an rms value of 6  $\mu\text{m}$  to each BPM offset.

The BBA procedure is similar to that described in Sec. III A but instead of injected-beam trajectory scans, orbit feedback is used to create orbit bumps around the BPM targeted for BBA and then adjust the orbit-bump excursion as needed. It is worth noting that creating ideal orbit bumps using three CMs with corrector settings based on the ideal lattice did not work reliably due to lattice errors and, more importantly, the CM limits.

We found that the most robust procedure to create a usable orbit bump was to use the orbit feedback to zero the orbit offset relative to the nominal centers of the non-BBA BPMs while ignoring the BPMs nearest to the BBA-BPM where the goal was to establish a 250- $\mu\text{m}$  orbit offset. Once the CM settings generating the intended orbit offset were found, we generated a family of ten intermediate-amplitude orbit bumps by scaling the settings of all the correctors by ten scaling factors chosen in the  $\pm 1$  interval. For each bump, the data are gathered with the quadrupole trim coils switched between  $K_1 = \pm 0.26 \text{ m}^{-2}$ , the maximum and minimum of the accessible range. The data analysis is analogous to that discussed in Sec. III A.

*BBA on quadrupoles.* All remaining BPMs are paired with neighboring quadrupole magnets. Similar to the previously described procedure, the orbit feedback with weighting factors is applied to create ten different orbit bumps at the considered BBA BPM with a maximum offset variation target of  $\pm 250 \mu\text{m}$ . The quadrupole gradient is varied to  $\pm 5\%$  of its nominal strength. In the case of combined function bending magnets, the horizontal corrector coil is used to compensate for the bending angle variation as explained below.

### C. Combined function magnets

The central-arc focusing quadrupoles are effectively combined-function magnets, installed with a small (up to 1.6 mm) offset to provide reverse bending. In order to allow for a  $\pm 5\%$  field-gradient tunability range to do optics correction and BBA, these magnets are equipped with horizontal dipole corrector coils (HCM) so that within that range, the bending angle can always be restored to nominal. However, both quadrupole and HCM calibration errors limit the precision with which the bending angle can be restored following a quadrupole-field adjustment. If the compensation is not perfect and during the BBA procedure, there is a residual bending angle error depending on the quadrupole set point, BBA will suffer from a systematic error in the horizontal plane.

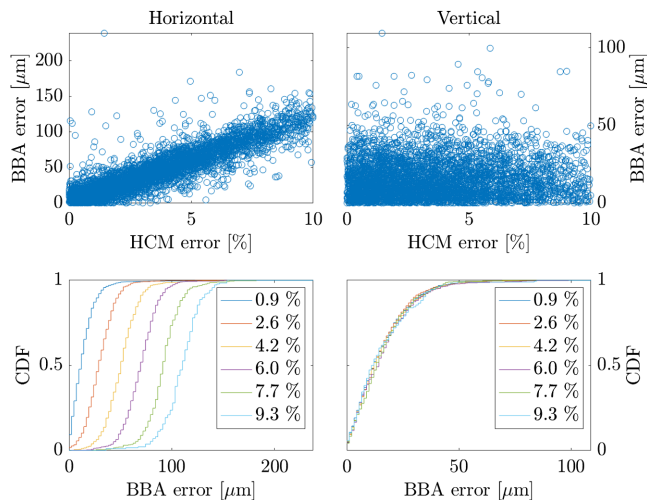


FIG. 9. Final BBA accuracy at combined function quadrupoles as a function of the HCM calibration error for the horizontal (left) and vertical (right) planes. The upper plots show the BPM offset w.r.t. the magnet centers for all BPMs at QF [4–6] (see Table II) for 200 error realizations in the commissioning simulation after three iterations of BBA (see Sec. IV G), when no CM or BPM calibration correction is applied. A clear correlation between the HCM calibration error and the BBA error is noticeable. The lower plots show the conditional CDFs of the BBA error for various HCM calibration error intervals. The effect is negligible for the vertical plane.

The impact of HCM calibration errors on the BBA accuracy is shown in Fig. 9. The figure reports the beam-based alignment of all the BPMs paired with the similar magnets  $QF4$ ,  $QF5$ , and  $QF6$  after three iterations of stored beam BBA in the commissioning simulation as explained in detail in Secs. IV F–IV H vs the HCM calibration error. Note that for this particular study, no CM or BPM calibration correction is performed during LOCO.

While there is no impact on the vertical plane, the correlation between the HCM calibration error and the horizontal BBA error is significant. A linear fit gives  $11.5 \mu\text{m}/\%$ .

Judging from the results of Fig. 9, it can be concluded that reliable correction of the HCM calibration factors is critical in order to achieve  $<30 \mu\text{m}$  rms BBA accuracy in the central arc. We also conclude that the HCM calibration errors will dominate the bending-angle error over the  $2 \times 10^{-4}$  magnet main-coil calibration error specified in Table III.

#### D. BBA outlier detection

For efficient statistical analysis, we need to be able to perform BBA automatically on a large set of lattice misalignment-error realizations. To this end, we found reliable detection of outliers to be critical. Ideally, it would reproduce a real-world machine operator’s ability to identify unfavorable BPM readings and BBA control parameters and repeat the measurements after introducing

suitable adjustments. As one can imagine, devising an algorithm capable of substituting manual intervention would be quite a challenge, perhaps something that may be amenable to future applications of machine learning. However, we successfully experimented with defining simple rules to flag flawed BPM readings and introducing plausible shortcuts to handle them.

We proceed in two steps. First, we identify a number of sensitive quantities that we need to monitor. One is the extent of the range over which the trajectory or orbit can be scanned. For example, if the beam gets lost at all but two preset amplitudes of injected-beam steering or close-orbit bumps, the linear fitting to find the quadrupole center from the downstream BPM data is prone to large errors. Another parameter of interest is the standard deviation of the magnet center as calculated from the downstream BPMs (red circles in Fig. 7). A very large value indicates that the signal-to-noise ratio is low; this can usually be circumvented by, e.g., a finer trajectory scan or modifying the phase advance slightly. In total, seven sensitive parameters are gauged to determine whether a BBA BPM can be deemed a failure, see the SC manual entry for the BBA routine for more details [12]. In particular, the BBA result is ignored for a certain BPM if the calculated offset change exceeds a user-defined threshold. The critical values of all the sensitive parameters, as used for this paper’s simulations, are documented in the example MATLAB® script [26].

The second step is applied after the BBA procedure for all BPMs within one group has been completed (e.g., all the BPMs paired with sextupole-magnet quadrupole trim coils). For the BPMs at which the BBA procedure has worked successfully, we take note of the rms value of the BPM alignment relative to the magnet center calculated using the simulated BBA. We then define the alignment to be attributed to the failed BPMs using a  $2\sigma$ -truncated Gaussian distribution with the rms value as calculated above. We conducted several spot-checks to verify that, for a given lattice error realization, the BPMs that fail by the criteria set by our outlier detection algorithm can indeed be cured by intervening manually and fine-tuning the control variables that affect the BBA outcome.

## IV. COMMISSIONING SIMULATION

Commissioning simulations have two goals: to validate the lattice design and correction schemes informing the error-tolerance specifications and to help prepare for the machine’s actual commissioning. The physics studies presented here are the first step toward developing detailed commissioning plans, which will be essential to meet the 1-year dark time goal.

The commissioning and lattice correction simulations are carried out using the Toolkit for Simulated Commissioning [15]. After a methodical evaluation of alternate paths and statistical analysis of outcomes, we have identified the following sequence as yielding the best performance:

- 
- (A) Improve initial transmission (Sec. IV A)
  - (B) Trajectory beam-based alignment (Sec. III A)
  - (C) Injected-beam static error correction (Sec. IV C)
  - (D) Sextupole ramp-up (Sec. IV D)
  - (E) rf correction (Sec. IV E)
  - (F) Closed-orbit correction (Sec. IV F)
  - (G) Closed-orbit beam-based alignment (Sec. IV G)
  - (H) LOCO-based optics correction (Sec. IV H)
  - (I) ID compensation (Sec. IV I)
- 

Steps B) and C) are performed in a loop with two iterations and steps F), G), and H) are repeated three times. Each step will be described in detail in the following. The implemented correction chain including all subroutines is available as a MATLAB® script on the SC home page [12].

Our approach is to devise automated trajectory/orbit and optics corrections that can be applied to a statistically significant population of lattice-error realizations without *ad hoc* intervention. The lattice performance is evaluated by monitoring the DA and Touschek lifetime, typically representing the results in terms of cumulative distribution function (CDF) and range of likely outcomes.

In the simulations, the lattice and injected-beam trajectory errors are assigned according to Tables III, V, VI, and XI–XIII, with each error source following a Gaussian distribution truncated at  $\pm 2\sigma$ . The injected bunch is represented by a six-dimensional  $\pm 3\sigma$ -truncated Gaussian distribution of 200 particles with rms sizes also reported in Table IV. The statistics is over a population of 500 error realizations. The automated correction chain was successful in 95% of error realizations.

The DA is generally evaluated on the momentum by 4D tracking over about 1000 turns. The quoted Touschek lifetime assumes a round beam and, unless otherwise stated, the design 1.15-nC bunch charge and Gaussian bunch profile with 4 times the natural rms bunch length to credit the harmonic cavities. However, early commissioning and operation are anticipated to be carried out without tuning in the harmonic cavities; therefore, the equivalent lifetime without harmonic cavities presupposes bunches with 1/4 of the design bunch charge (or  $\sim 0.3$  nC). Synchrotron radiation is generally included in all relevant lattice elements.

The sequence of commissioning steps and correction procedures is detailed below. Commissioning starts with the rf cavities and sextupole magnets switched off.

### A. Improve initial transmission

At the start of commissioning before any correction, on average, the beam is not expected to get past the first arc. This assumes that the beam follows the ideal trajectory through the ATS transfer line and that systematic and random errors are applied to the injected beam at the exit of the swap-out kicker according to Table III. Indeed, the left-hand image of Fig. 10, reporting the cumulative distribution

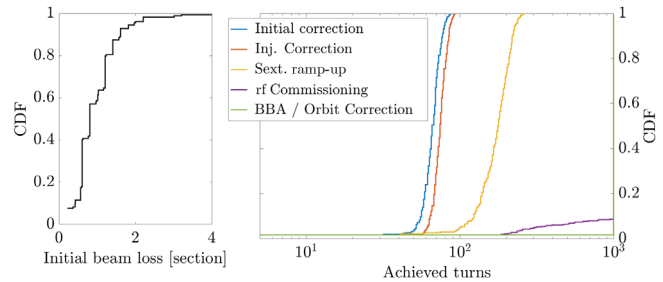


FIG. 10. Beam transmission at various steps of the correction chain. The left-hand plot shows that on day 1 of commissioning without any correction, the beam will almost certainly get lost within the first two arcs. The colored lines in the right-hand plot indicate the beam transmission after performing the correction steps detailed in the inset.

function of beam-loss locations over a number of lattice and injected-beam error realizations, shows that almost certainly the beam will get lost within the first two sectors.

The first step in the correction chain is to establish transmission through one turn using the same feedback-like iterative trajectory correction approach proposed for the AR commissioning and described in detail in Sec. IV B in [15]. Upon “stitching” the BPM readings in the second turn to the readings of the first turn and progressively increasing the number of BPM readings to be utilized in the trajectory correction algorithm, the beam is found to survive about 60 turns on average (blue curve in the right-hand image of Fig. 10).

### B. Trajectory BBA

As shown in Fig. 5, decreasing the relatively large initial BPM offsets considerably is critical for reliably achieving stored beam.

At this stage of commissioning, the perturbed lattice properties differ significantly from those of the ideal model. With beam transmission safely exceeding two turns, as a further step toward bringing the lattice to behave closer to the design model, model-independent, trajectory-based BBA on the quadrupoles as described in Sec. III A is carried out.

A total of two iterations each followed by trajectory feedback and static injection error correction as described in Sec. IV C are carried out. The results of the BBA simulation are shown in Fig. 11 and Table VIII. The achieved determination of the BPM offset error relative to the adjacent quadrupole magnets is about  $60 \mu\text{m}$  and  $40 \mu\text{m}$  rms in the horizontal and vertical planes, respectively, which meets the  $50\text{-}\mu\text{m}$  requirement identified in Sec. III A.

### C. Injected-beam static error correction

After the BPM offsets have been adjusted to credit trajectory BBA, the static injection error can be corrected.

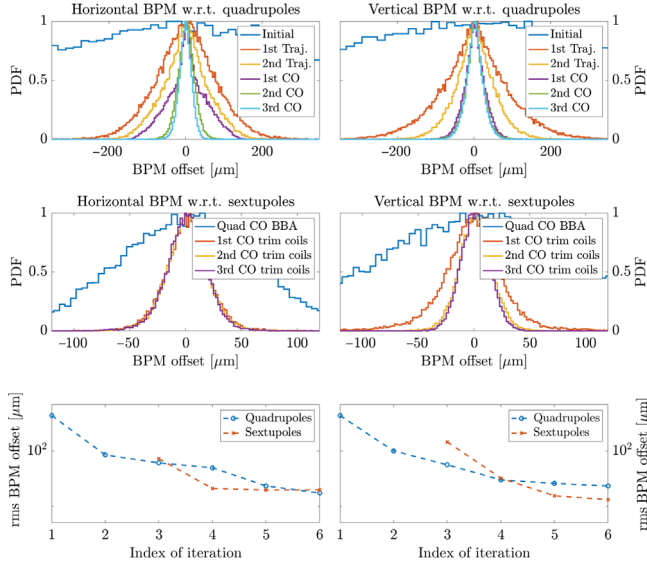


FIG. 11. BBA results after completing two trajectories and three closed-orbit correction iterations, as indicated in the insets. The figures show the statistical distributions of the BPM alignment errors for BBA conducted on the BPMs adjacent to quadrupole (top) and sextupole (middle) magnets. The bottom images report the rms of the distributions shown above at the various correction stages (Index = 1 corresponds to the initial BPM mechanical misalignment errors; Index = 2 to the errors after the first trajectory-correction iteration, and so on). Left (right) pictures are for alignment errors in the horizontal (vertical) plane. Note that BBA on sextupoles (red curves) is done only on stored-beam BBA, and hence Index  $\geq 3$  (see Sec. IV G).

A periodicity-1 orbit is generated with the trajectory feedback using the BPM readings of the first turn as a reference trajectory for the second turn, with the algorithm trying to force a BPM reading from the first turn to equal the reading from the second turn. Once the procedure has converged, the readings from the BPM immediately

TABLE VIII. BBA results throughout the commissioning simulation for BPMs paired with quadrupoles (upper table) and chromatic sextupoles (lower table). Shown are the BPM offsets with respect to the corresponding magnet centers after various BBA procedures.

Name	Horizontal [ $\mu\text{m}$ ]	Vertical [ $\mu\text{m}$ ]
Initial	442	441
First trajectory	85	101
Second trajectory	61	56
First CO	50	30
Second CO	23	26
Third CO	17	23
Quad CO BBA	72	147
First CO trim coils	21	32
Second CO trim coils	20	15
Third CO trim coils	20	13

upstream and the BPM immediately downstream of the injection point are used to deduce the injected-beam trajectory, thus allowing for its correction (using the ATS transfer-line correctors and pulsed elements; this part, however, has not been simulated yet). The injection error is thereby decreased to  $80 \mu\text{m}$  and  $33 \mu\text{rad}$  for the horizontal and  $76 \mu\text{m}$  and  $30 \mu\text{rad}$  for the vertical planes.

#### D. Sextupole ramp-up

At this point, the large natural chromaticities are limiting the beam transmission and degrading the multiturn BPM readings. Ramping-up the sextupoles in steps of 1/10 of their nominal strength while applying the previously described trajectory feedback after each step works reliably and increases the overall beam transmission significantly (see the yellow curve in the right-hand image of Fig. 10).

#### E. rf commissioning

The implemented rf cavity phase and frequency correction routines make use of the fact that a turn-by-turn (TBT) energy variation will result in a TBT horizontal BPM variation due to dispersion; these routines are described in detail in Sec. IV-D in [15]. rf phase and frequency correction are performed in a loop with three iterations, starting with the phase. After the first phase correction, a betatron-tune scan (see Sec. IV-E in [15]) is performed to ensure at least 50 turns of transmission for the subsequent rf frequency correction. This tune scan rarely comes into play (typically  $\leq 3/500$  error realizations) and the quadrupole set-point variation is less than 0.1%. It is worth noting, however, that the tune scan is significantly more critical to the overall correction chain success in the presence of looser error tolerance specifications and therefore detrimental in order to explore the sensitivity of the correction chain performance over a wider error range.

The energy and phase error between the closed orbit and the injected beam throughout the rf correction loop are plotted in Fig. 12.

Most lattice error realizations  $>95\%$  are now consistent with a stored beam surviving at least 1k turns (purple curve in the right-hand image of Fig. 10), setting the stage for more refined corrections.

#### F. Closed-orbit correction

At this point, the beam transmission is sufficient to allow for the reliable measurement of the closed orbit. Therefore, the simulation is switched from turn-by-turn to orbit mode. Orbit feedback is applied including dispersion, thus with the rf frequency as an adjustable parameter. Closed orbit dispersion and the orbit response matrix are calculated from the designed lattice. For better convergence, an appropriate scaling factor is applied to weight the orbit response to rf frequency variations vs the response to the correctors.

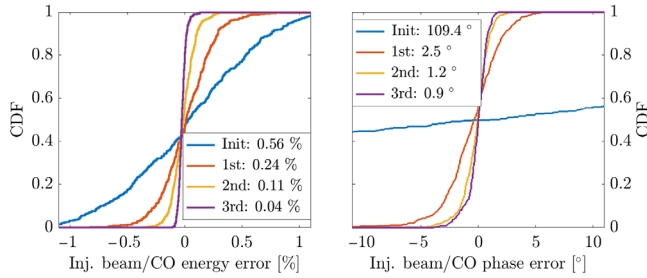


FIG. 12. Results of the rf commissioning procedure. Shown is the difference between the closed orbit energy (left) and phase (right) with respect to the injected beam, both initially (blue) and after each of the three iterations. The rms values are shown in the inset.

A weighting factor of  $10^7$  Hz/rad between the rf frequency and CM was found to provide good results.

The correction is performed in a loop successively decreasing the parameter  $\alpha$  in the Tikhonov regularization used to calculate the pseudoinverse matrix [11]. The loop is halted when the rms BPM reading stops decreasing.

Note that if orbit correction is applied within optics correction (Sec. IV H) or ID compensation (Sec. IV D), a weighting factor of 10:1 is applied on the BPM readings adjacent to the chromatic sextupole magnets vs all other BPMs to enforce the orbit feedback to prioritize the orbit correction in the sextupole magnets. Only when orbit correction is applied before a BBA routine (Sec. IV G), the weighting factors are equal for all BPMs.

The results reported in Fig. 13 show that the final rms orbit variation in the sextupole magnets is about 32 and 26  $\mu\text{m}$  rms for the horizontal and vertical planes, respectively.

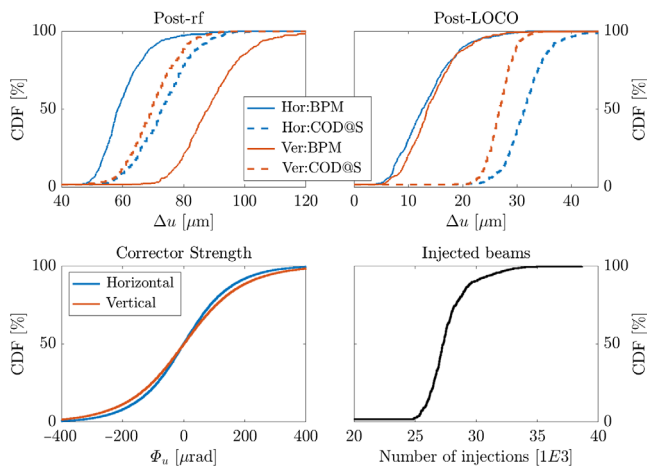


FIG. 13. Machine status after applying final orbit correction. The lower plots show the CDFs of the number of required beam injections (right) and the required corrector strength (left) of all CMs of all error seeds. The upper plots show the rms value of the BPM readings (solid) and COD in SF/SD magnets (dashed) before and after applying three iterations of Secs. IV F–IV H (rms over each error seed).

## G. Closed-orbit BBA

Having established a closed orbit, the closed-orbit BBA can now be carried out on both the quadrupole and the sextupole magnets as described in Sec. III B.

It is well known that the accuracy of model-independent BBA depends on the orbit error. Furthermore, as described in Sec. III C, the BBA accuracy in the arcs depends significantly on the calibration errors of the HCMs. Since those can only be determined after the lattice optics errors are sufficiently corrected, it is necessary that BBA, orbit correction, and optics correction are applied in a loop recursively. Typically, the algorithm converges reasonably well after three iterations, as can be seen in Fig. 11 and Table VIII.

As described above, the sextupole coils of the targeted sextupole magnet are switched off during the BBA measurement to minimize saturation effects. The resulting lifetime degradation is significant, but  $>1$  min, as found in all analyzed cases, would be sufficient for orbit measurements. The lifetime here was calculated assuming a bunch population equal to 1/4 of nominal (and no HHC-induced bunch lengthening).

## H. LOCO-based linear optics correction

LOCO-based linear optics correction [28,29] is done through a sequence of nine distinct steps. It is understood that each LOCO step detailed below is followed by orbit correction, using the algorithm described in Sec. IV F.

Initially, a response matrix (RM) is measured using all available BPMs (226) and corrector magnets ( $294 + 216$ ), including the HCMs on the main combined-function bending magnets (which have no vertical correctors). The CM kick angles are assigned based on the ideal-lattice RM so that on average the BPM readings vary in steps of about 50  $\mu\text{m}$ . For dispersion measurement, the rf frequency is varied by 1500 Hz to produce about 50  $\mu\text{m}$  BPM reading differences.

Both the orbit RM and the dispersion are measured bidirectionally with a total of three CM and rf steps. In the optics correction steps where the dispersion is included, we found that weighting it with a factor of 5 in both planes gives the best results.

While in general, the orbit in all SC functions is calculated with the AT function `findorbit6()`, which finds the fixed point of the complete one-turn 6D-map, LOCO determines the orbit RM based on the linear approximation of the 4D transfer matrices between CMs and BPMs. The LOCO approach has the advantage of speeding up the calculation by 2 orders of magnitude. However, it has to be noted that because the corrector magnets in the ALS-U SR are not stand-alone but are incorporated in the lattice magnets (quadrupoles and sextupoles), there is a significant dipole feed-down term from the magnet main field when the trajectory through the magnet changes in response to the embedded corrector. This effect

is not included in the linear response matrix calculator of the LOCO routine. The result is equivalent to an apparent CM calibration error between the SC toolkit and LOCO. Due to the large quadrupole magnet strengths, this calibration offset can be as large as 30% and has to be accounted for when performing LOCO, e.g., by using a precalculated table of adjustments when applying the CM calibration error fits to the toolkit lattice.

The first optics correction step includes all QF1 and QD1 quadrupole magnets while at first ignoring coupling (off-diagonal response matrix blocks) and diagnostic errors. In the second step the magnet families, QF4, QF5, and QF6 are added as fit parameters, while in the third step, dispersion and coupling are included and all skew quadrupole correctors are engaged. Starting with the fourth step, chromaticity correction is applied and will be repeated at each subsequent step.

The fifth step does not involve any quadrupoles but only the fitting of the BPM and CM calibration factors. In order to get a better agreement, the orbit RM within LOCO is calculated using `findorbit6()` for this step.

The calibration factors are fit in a five-substep process; first, only the CM calibration errors are fitted, then only the BPM calibration errors (second substep). This is repeated (third and fourth substep) and only at the fifth substep, both BPM and CM calibration errors are fitted simultaneously. In most cases, this detailed process is not needed but it was found to be very robust and therefore most suitable when processing a large set of error seeds.

From this point on the BPM and CM, calibration factors remain unchanged. After two more LOCO steps with the settings as described for the fourth step, the two final steps also include all B2 and B3 quadrupole gradients.

As described before, orbit correction, BBA, and optics correction are applied in a loop with three iterations. The end result is shown in Fig. 14. Beta beat is between 1% and 5%, the DA gets restored sufficiently well (see Fig. 15), and the required normal and skew quadrupole strengths are acceptable.

### I. ID compensation

Together with orbit deviation and magnet errors, in a relatively low-energy machine like the ALS, the IDs represent an important source of undesired perturbations to linear optics. These need to be effectively corrected to avoid excessive DA and MA degradation.

While the ultimate goal is to represent each ID in the SR with its appropriate model, the results discussed here are based on a reduced model encompassing only the eight strongest IDs: COSMIC, LEDA, TENDER, U114, XType, EPU35, EPU90, and EPU50, see Table IX. The strongest ID, U114, is modeled by a series of SBEND elements, whereas all other IDs are represented by kick maps.

Because the ID settings vary by users' demand, the correction method should be practical and robust. After

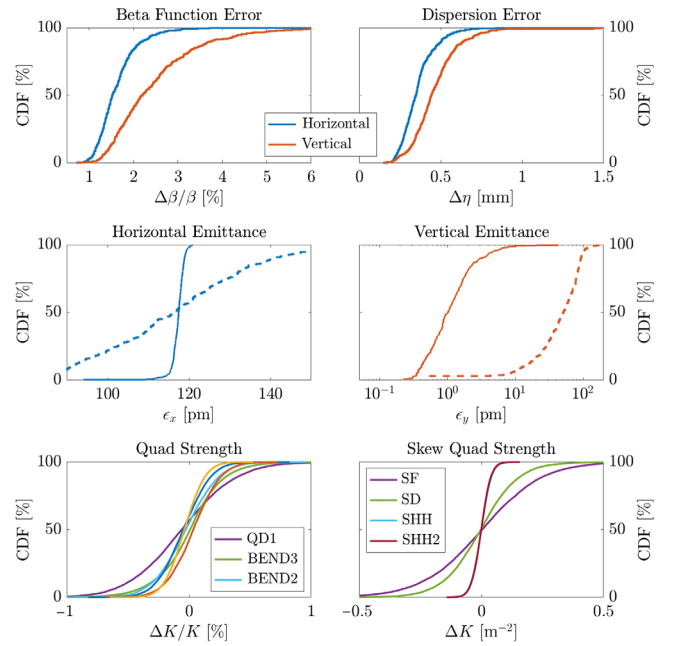


FIG. 14. Visualization of LOCO results. Cumulative distribution functions (CDF) of beta beat, dispersion error, and emittance each before (dashed) and after (solid) optics correction in the upper four plots. The lower two plots show the final relative quadrupole set-point deviation from the design value (left) and the required skew quadrupole strength (right).

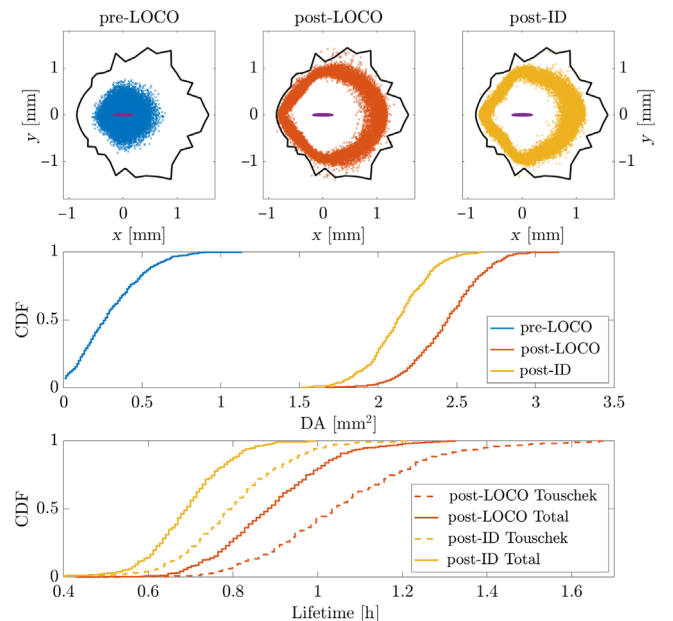


FIG. 15. DA (top and center) and lifetime (bottom). The comparison is between before (blue) and after (red) performing optics correction, and after including and compensating for the IDs (yellow). In the upper images, the solid curve is the ideal lattice DA, and the purple ellipses indicate the injected beam size ( $3\sigma$ ). In the bottom image, the dashed curves are the CDF for the Touschek lifetime only; the solid curves are the CDF for the total beam lifetime (Touschek and vacuum).

TABLE IX. Undulator parameters.

ID name	$\lambda_u$ (mm)	No. of periods	Minimum gap (mm)
EPU38 (COSMIC)	38	44.5	12.5
U15 (LEDA)	15	131	4.5
EPU35	35	52.5	12
EPU50	50	89	14
EPU90	90	20.5	14.5
U114	114	29	12.5
U19 (new)	19	210	4
X32 (new)	32	123.5	9.5

experimenting with various alternatives, the global correction method described in Ref. [30] was found to be the most effective. The method seeks to minimize the betatron-function errors at, and the betatron phase-advance errors between, the chromatic sextupoles (the main sources of the machine nonlinearities). The figure of merit is constructed based on these errors: a weighting of 100:1 between phase advance and beta-beat, respectively, was found to provide the best results.

The partial derivatives of the merit function with respect to changes in every quadrupole magnet strength are calculated and stored in a response matrix. Subsequently, the IDs are inserted in the ideal lattice and an SVD-based algorithm is used to determine the required quadrupole set-point change to minimize the merit function. We studied different regularization methods (cutting singular values and Tikhonov regularization) and found that the Tikhonov regularization with regularization parameter  $\alpha = 1$  provided the best results.

The identified quadrupole set-point change is then applied to the lattice including all errors. Subsequently, three iterations of orbit feedback, tune, and chromaticity correction are performed. As in Sec. IV H, it is hereby assumed that the tune and chromaticity corrections at this point of the commissioning will be straightforward to perform. Therefore, it is not necessary to simulate the beam-based correction process; instead, a MATLAB® based `fminsearch()` with target precision of  $1 \times 10^{-3}$  is used to realize the intended correction.

Results for the DA and total lifetime before and after ID compensation are shown in Fig. 15. While the DA reduction is modest, a significant lifetime reduction due to ID perturbations of about 35% is notable. The total lifetime is above the 0.5 h requirement in 98% of all cases with an average value of 0.70 h (0.81-h Touschek lifetime only).

## V. FINE-TUNING OF LATTICE CORRECTION

Our effort has so far focused on defining and tuning the correction procedures that maximize performance and minimize failure in a statistical sense when applied to a wide range of error specifications. While this approach has

obvious advantages, it may imply an excessively conservative estimate of the most likely performance to be expected of the built-machine lattice. Once the machine is built, tailored correction procedures and further optimization can be expected to improve its performance.

In this spirit, we investigate the effect of optimizing the Touschek lifetime by choosing individual LOCO horizontal and vertical dispersion weight factors for each error seed and subsequently fine-tuning the harmonic sextupole families in the following sections.

### A. LOCO dispersion weight scan

Common fine-tuning parameters for linear optics correction are the horizontal and vertical dispersion weights with respect to the orbit response measurements. While a mathematically meaningful way is to weigh the dispersion with the square root of the numbers of CMs (thus about 20 for the ALS-U SR), the actual weight that yields the best corrected lattice performance is not clear *a priori*. As mentioned in Sec. IV H, we found that weighting factors of 5 in both planes tended to give the best results statistically. However, for individual error realizations, these numbers may differ.

In order to investigate the effect of individually fine-tuned dispersion weights on the lattice correction capability, we randomly picked 50 error realizations from the pool described above and carried out the correction steps of Secs. IV F to IV I with different horizontal and vertical dispersion weights ranging from 0.1 to 20. For each error realization, we evaluated the Touschek lifetime before and after ID compensation for each pair of dispersion weights.

Results are shown in Fig. 16. While most of the error realizations can be corrected best with dispersion weight

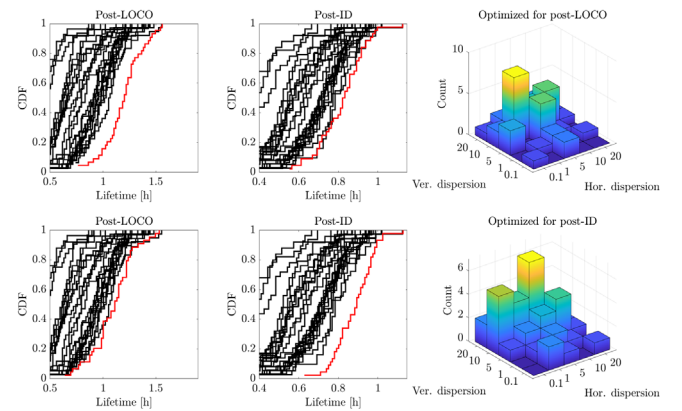


FIG. 16. Lifetime optimization using LOCO dispersion weights. The histogram in the right plots shows the value of horizontal and vertical dispersion weight yielding the best lifetime without IDs (upper row) and after ID compensation (lower row). The black lines in the left and center plots show the lifetime for each pair of dispersion weights, the red lines indicate the lifetime when for each error realization the best value is chosen. The optimum dispersion weights with and without IDs differ.

$\geq 5$ , for some error seeds, very small values yield better performance. By choosing the dispersion weight for each lattice individually, the lifetime can be improved by about 10% with and without IDs, respectively, compared to the baseline. However, it is worth noting that dispersion weights which produce the best results without IDs do not necessarily maximize the lifetime after IDs are included. When optimizing with IDs, the rms lifetime increase is about 11 min.

### B. Harmonic sextupole scan

A subsequent optimization against specific error seeds is carried out by tuning the two harmonic-sextupole families.

We use the 50 post-ID lattices with optimized LOCO dispersion weight (red curve in the bottom right plot of Fig. 16). For each lattice, the SHH and SHH2 harmonic sextupole strength is varied on a  $[6 \times 8]$  grid while applying chromaticity, tune, and orbit correction. The Touschek lifetime is calculated at each step.

An example of lifetime vs sextupole strength plot can be found in Fig. 17. It is worth noting that the actual pattern differs significantly for different error seeds and in some cases, there was no lifetime improvement possible at all. As indicated in Fig. 17, it might be possible to significantly improve the performance by using a finer grid. On the downside, however, the steep change of lifetime for small changes in harmonic sextupole strength for some lattices might point to potential operational difficulties maintaining the optimum lifetime when the ID settings change.

For the grid points and error seeds used in this study, the average lifetime can be increased by 6 min or 7% rms compared to the dispersion weight optimization. The final average Touschek lifetime is 0.97 h and significantly exceeds 0.81-h result of Sec. IV I. It is worth noting that

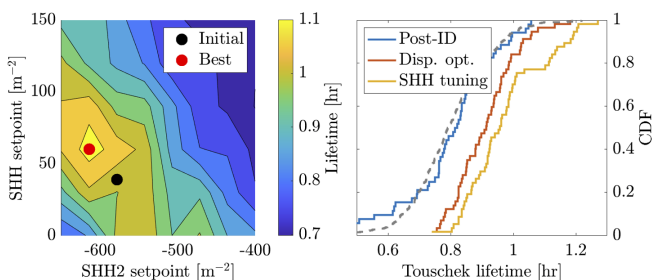


FIG. 17. Touschek lifetime optimization by harmonic-sextupole scans following the dispersion-weight optimization. The left plot shows the lifetime as a function of the SHH and SHH2 set points for one choice of error seed. In this example, the lifetime can be increased from 0.94 to 1.12 h. The right plot shows the distribution of Touschek lifetime after regular ID compensation in blue for the selected error seeds (gray curve shows the distribution of all error seeds, see Sec. IV I), after optimizing the post-ID lifetime using LOCO dispersion weights (red curve, see Sec. V A) and after tuning the sextupole magnets (yellow curve).

the dynamic aperture did not degrade during the dispersion weight and sextupole optimization procedures.

## VI. CONCLUSIONS

In this paper, we described the development of a start to finish commissioning simulation of the ALS-U Storage Ring including a comprehensive and realistic set of errors and correction steps. After demonstrating the importance of minimizing closed-orbit deviations in the sextupole magnets for the final machine performance, emphasis has been placed on the development of a reliable BBA routine, successfully reducing the BPM offset to the sextupole magnets to  $\leq 20 \mu\text{m}$ . We were able to show that the design goal of a final beam lifetime  $\geq 0.5$  h can be achieved with tailored linear-optics correction and ID compensation. Finally, we showed that fine-tuning of the correction chain based on specific lattice error realizations holds the potential for further improvements.

## ACKNOWLEDGMENTS

We would like to thank Simon Leemann, Changchun Sun, Michael Ehrlichman, Michael Borland, Vadim Sajaev, Timur Shaftan, and Philipp Amstutz for valuable discussions and feedback on this work. This work was supported by the Director of the Office of Science of the U.S. Department of Energy under Contract No. DEAC02-05CH11231.

## APPENDIX: ADDITIONAL MAGNET PARAMETERS

For completeness in this Appendix, we report the magnet parameters for the three sectors with hard bends, Table X, the systematic and random multipole errors for the hard bends, Table XI, and the systematic multipole errors associated with the dipole and skew-quadrupole corrector coils, Tables XII and XIII, respectively.

In Table X, QD2 and QD3 (with  $L = 0.1325$  m effective length) is the pair of defocusing quadrupoles flanking each hard bend. The hard bends' effective length is  $L = 0.135$  m.

TABLE X. Magnet parameters for the three sectors with hard bends (HB). Only the magnets with settings different from those in the normal sectors are reported.

	QF3/QF4/QF5/QF6	QD2/QD3
$K_1$ ( $\text{m}^{-2}$ )	10.54/15.39/16.34/16.31	-14.39/ - 14.87
$\theta$ (deg)	-0.0063/ - 0.429/ -0.429/ - 0.429	0/0
	B2/B3	HB
$K_1$ ( $\text{m}^{-2}$ )	-7.098/ - 7.098	0
$\theta$ (deg)	3.648/3.763	3.763

TABLE XI. Hard bends' systematic and random higher-order multipole errors relative to the design ( $B_1 = 3.247$  T) dipole field component in units of  $10^{-4}$  (reference radius  $R = 3$  mm).

$n$	2	3	4	5	6	7	8	9	10
Systematic $b_n$	-14.	8.3	29	-61	-11	14	4.2	3.7	-1.2
Random $b_n$	-2	-3.6	-2.4	-3.6	-0.74	-0.31	-0.25	-0.37	-0.28
Random $a_n$	2.1	2.8	0.79	1.2	0.55	0.33	0.14	0.2	0.12

TABLE XII. Systematic higher-order multipole errors associated with the dipole trim/corrector coils correcting in the horizontal (top) and vertical (bottom) planes. The correctors are embedded in the bending (B2/B3), quadrupole (Q), and sextupole (SF/SD/SH) magnets. Multipoles are in units of the corrector dipole field ( $b_1 = 1$  and  $a_1 = 1$  for horizontal and vertical correctors).

	B2/B3	Q	SF/SD	SH
$b_3$	0.037	0.12	0.0	0.0
$b_5$	-0.00037	0.0013	0.018	0.012
$b_7$	0.00023	-0.00066	-0.00042	-0.00036
	Q	SF/SD	SH	
$a_3$	0.12	0.0	0.0	
$a_5$	-0.0013	0.018	0.012	
$a_7$	-0.00055	0.00042	0.00036	

TABLE XIII. Systematic skew-multipole errors from the skew-quadrupole corrector coils in the sextupole magnets in units of the corrector skew-quadrupole field ( $a_2 = 1$ ). The normal multipoles are negligible.

	SHH	SHH2	SF/SD
$a_4$	0.12	0.12	0.14
$a_6$	0.00015	0.00036	0.000011
$a_8$	0.00085	0.00094	0.00089

- [1] A. Allezy *et al.*, The Advanced Light Source Upgrade Project: Final Design Report, Lawrence Berkeley National Laboratory, Berkeley, 2022 (unpublished).
- [2] P. F. Tavares *et al.*, Commissioning and first-year operational results of the MAX IV 3 GeV ring, *J. Synchrotron Radiat.* **25**, 1291 (2018).
- [3] J. Biasci *et al.*, A low emittance lattice for the ESRF, *Synchrotron Radiat. News* **27**, 8 (2014).
- [4] A. Rodrigues *et al.*, Sirius Status Update, in *Proceedings of the 10th International Particle Accelerator Conference, IPAC-2019, Melbourne, Australia* (JACoW, Geneva, Switzerland, 2019).
- [5] M. Borland *et al.*, The upgrade of the Advanced Photon Source, in *Proceedings of the 9th International Particle Accelerator Conference, IPAC-2018, Vancouver, British Columbia, Canada* (JACoW, Geneva, Switzerland, 2018), pp. 2872–2877, [10.18429/JACoW-IPAC2018-THXGBD1](https://doi.org/10.18429/JACoW-IPAC2018-THXGBD1).
- [6] M. Dehler *et al.*, Conceptual design for SLS-2, in *Proceedings of 60th ICFA Advanced Beam Dynamics Workshop on Future Light Sources, FLS2018, Shanghai, China* (JACoW, Geneva, Switzerland, 2018).
- [7] I. P. S. Martin *et al.*, Diamond-II storage ring developments and performance studies, in *Proceedings of the 13th International Particle Accelerator Conference, IPAC-2022, Bangkok, Thailand*, paper TUPOMS033, [10.18429/JACoW-IPAC2022-TUPOMS033](https://doi.org/10.18429/JACoW-IPAC2022-TUPOMS033).
- [8] A. Loulergue *et al.*, Baseline Lattice for the Upgrade of SOLEIL, in *Proceedings of the 9th International Particle Accelerator Conference, IPAC-2018, Vancouver, British Columbia, Canada* (JACoW, Geneva, Switzerland, 2018), [10.18429/JACoW-IPAC2018-THPML034](https://doi.org/10.18429/JACoW-IPAC2018-THPML034).
- [9] Emanuel Karantzoulis *et al.*, Elettra, present and future, in *Proceedings of the 10th International Particle Accelerator Conference, IPAC-2019, Melbourne, Australia* (JACoW, Geneva, Switzerland, 2019), [10.18429/JACoW-IPAC2019-TUPGW031](https://doi.org/10.18429/JACoW-IPAC2019-TUPGW031).
- [10] Ilya Agapovand *et al.*, Status of the PETRA IV project, in *Proceedings of the 10th International Particle Accelerator Conference, IPAC-2019, Melbourne, Australia* (JACoW, Geneva, Switzerland, 2019), [10.18429/JACoW-IPAC2019-TUPGW011](https://doi.org/10.18429/JACoW-IPAC2019-TUPGW011).
- [11] Thorsten Hellert, Philipp Amstutz, Christoph Steier, and Marco Venturini, An Accelerator Toolbox (AT) Utility for simulating the commissioning of storage-rings, in *Proceedings of the 10th International Particle Accelerator Conference, IPAC-2019, Melbourne, Australia* (JACoW, Geneva, Switzerland, 2019), paper TUPGW021, 2019.
- [12] Toolkit homepage: <https://sc.lbl.gov>.
- [13] A. Terebilo, in *Proceedings of Workshop on Performance Issues at Synchrotron Light Sources Berkeley, CA, 2000* (2001).
- [14] V. Sajaev, Commissioning simulations for the Argonne Advanced Photon Source upgrade lattice, *Phys. Rev. Accel. Beams* **22**, 040102 (2019).
- [15] Thorsten Hellert, Philipp Amstutz, Christoph Steier, and Marco Venturini, Toolkit for simulated commissioning of storage-ring light sources and application to the advanced light source upgrade accumulator, *Phys. Rev. Accel. Beams* **22**, 100702 (2019).
- [16] Marco Venturini and Thorsten Hellert, Particle-ray tracing through dynamics and misaligned lattice elements, *Nucl. Instrum. Methods Phys. Res., Sect. A* **1044**, 167487 (2022).
- [17] Zeus Marti (private communication).
- [18] M. Apollonio *et al.*, Commissioning strategy for Diamond-II, in *Proceedings of the 12th International Particle*

- Accelerator Conference, IPAC-2021, Campinas, SP, Brazil* (JACoW, Geneva, Switzerland), paper MOPAB063, [10.18429/JACoW-IPAC2021-MOPAB063](https://doi.org/10.18429/JACoW-IPAC2021-MOPAB063).
- [19] O. Blanco-Garcia *et al.*, Status of the soleil upgrade lattice robustness studies, *Proceedings of the 13th International Particle Accelerator Conference (IPAC'22)* (JACoW Publishing, Geneva, Switzerland, 2022), pp. 433–436, [10.18429/JACoW-IPAC2022-MOPOTK004](https://doi.org/10.18429/JACoW-IPAC2022-MOPOTK004).
- [20] Sara Dastan (private communication).
- [21] Aanma Kahn (private communication).
- [22] Thorsten Hellert *et al.*, Error analysis and commissioning simulation for the PETRA-IV storage ring, in *Proceedings of the 13th International Particle Accelerator Conference, IPAC-2022, Bangkok, Thailand* (JACoW, Geneva, Switzerland, 2022).
- [23] F. Schmidt, MAD-X PTC integration, *Conf. Proc. C* **0505161**, 1272 (2005).
- [24] G. Portmann, D. Robin, and L. Schachinger, Automated beam based alignment of the ALS quadrupoles, *Conf. Proc. C* **950501**, 2693 (1996), <https://inspirehep.net/literature/400256>.
- [25] Xiaobiao Huang, *Beam-Based Correction and Optimization for Accelerators* (CRC Press, Boca Raton, 2020), [10.1201/9780429434358](https://doi.org/10.1201/9780429434358).
- [26] Path to full storage ring example: [https://github.com/ThorstenHellert/SC/tree/master/applications/ALSU\\_SR](https://github.com/ThorstenHellert/SC/tree/master/applications/ALSU_SR).
- [27] P. Emma, Beam based alignment of sector-1 of the SLC linac, Report No. SLAC-PUB–5787, 1992.
- [28] J. Safranek, Experimental determination of storage ring optics using orbit response measurements, *Nucl. Instrum. Methods Phys. Res., Sect. A* **388**, 27 (1997).
- [29] J. Safranek, G. Portmann, A. Terebilo, and C. Steier, MATLAB based LOCO, in *Proceedings of the 8th European Particle Accelerator Conference, EPAC-2002, Paris, France* (European Physical Society, Geneva, 2002), pp. 1184–1186.
- [30] T. V. Shaftan, J. Bengtsson, and S. L. Kramer, Control of dynamic aperture with insertion devices, *Conf. Proc. C* **060626**, 3490 (2006), <https://inspirehep.net/literature/739523>.